A self-calibration scheme to monitor long-term changes in linear and rotary axis geometric errors

Shota Onishi[a], Soichi Ibaraki[a,*], Tomoyasu Kato[a], Masashi Yamaguchi[b], Takao Sugimoto[c]

[a] *Graduate School of Advanced Science and Engineering, Hiroshima University, Kagamiyama 1-4-1, Higashihiroshima, 739-8527, Hiroshima, Japan.*
[b] *Kawasaki Technology, Co., Ltd., Japan.*
[c] *Kawasaki Heavy Industries, Ltd., Japan.*

Abstract

A calibration scheme of position and orientation errors of rotary axis average lines based on touch-trigger probing is widely available on many commercial five-axis machine tools. Such a measurement is influenced by error motions of both linear and rotary axes. This paper proposes a novel scheme to separately identify linear and rotary axis geometric errors by using a touch-trigger probe and an uncalibrated test piece. Whereas the proposed scheme is based on well-developed self-calibration schemes for the circularity measurement, an original contribution is that it is applied to separate linear and rotary axis geometric errors. Two case studies are presented. First, the proposed tests are performed on the same five-axis machine tool for half a year to observe a long-term change in linear and rotary axis geometric errors. The second case study investigates the influence of room temperature change on linear axis and rotary axis error motions.

Keywords: Geometric error, Five-axis machine tool, Touch-trigger probe, Self-calibration, Error separation

*Corresponding author
Email addresses: m212705@hiroshima-u.ac.jp (Shota Onishi), ibaraki@hiroshima-u.ac.jp (Soichi Ibaraki)

1. Introduction

Recent advances in sensor technologies, automated data acquisition systems and communication links have provided new opportunities for implementing machine tool condition monitoring systems [1]. According to [1], current machine tool condition monitoring systems target two aspects of areas; the machining process and machine tool systems. In the latter, long-term change in quasi-static geometric accuracy of linear and rotary axes is a major contributor to the change in the machining accuracy. Environmental change, particularly the thermal change, is a major cause for the change in linear axis geometric errors [2]. However, thermal change is not a sole cause for long-term changes. Linear axis error motions can change due to the change in the friction on a guideway or a ball screw [3]. For a long linear axis, the change in the ground geometry or stiffness can significantly change the straightness error motion in a long term.

In civil engineering, long-term continuous condition monitoring for large buildings or bridges is widely available. Typically, electrical resistance strain gauges and fiber-optic Bragg grating sensors are used to measure the stress distribution [4]. A few researchers presented the application of strain gauges [5] or Fiber Bragg Grating sensors [6] to the estimation of linear axis error motions in a machine tool. Since they do not directly measure error motions, it is typically difficult to ensure sufficiently high measurement accuracy required for machine tools. Thus, several periodic monitoring schemes of linear axis error motions, commercially available from machine tools manufactures or maintenance service providers (e.g. Okuma Corp. and NIDEC Machine Tool Corp.), are based on direct measurement of three-dimensional (3D) positioning errors by using a touch-trigger probe and an artefact. When the geometry of an artefact, typically a ball array, as is often used in the verification of coordinate measuring machines (CMMs) [7], is pre-calibrated, the measured positions by a touch-trigger probe give the machine tool's 3D positioning errors.

For machine tools with rotary axes, one of the geometric error sources is an assembling error of rotary axis, which appears as the position and orientation

errors of rotary axis average lines [8]. Various methods have been actively researched to identify the position and orientation errors of rotary axis average lines, and been in practical use[9], including the R-test [10],[11],[12],[13],[14], the ball-bar tests [15], and the method utilizing a sphere and a touch-trigger probe [16],[17],[18],[19]. In particular, the probing-based schemes are commercially available from many machine tool builders (see Fig. 2).

All the methods reviewed above measure the relative displacement between the spindle and the work table. A critical issue is that they cannot separate linear axis geometric errors from rotary axis geometric errors in principle. As a result, many previous studies reviewed above assume that linear axis geometric errors are negligible. Bringmann and Knapp [20] discussed in details the influence of linear axis error motions on the uncertainty in the estimation of position and orientation errors of rotary axis average lines. They stated that "it can be remembered that errors like tilting, roll, run-outs or hysteresis do not only cause direct errors on a work-piece when machining, but are also increasing the uncertainties in the identification of the main geometric errors ... ('You have to pay for bad axes twice!')."

In ISO 230-2 [21] and 230-7 [8], rotary axis error motions can be measured independently from a linear axis. For example, the angular positioning error motion can be measured by using a laser interferometer and a reference polygon mirror or indexing table [21]. The radial, axial, and tilt error motions are measured by measuring the displacement of a cylindrical artefact [8]. However, these methods require the measured artefact installed on the rotary axis centerline. It requires careful setup, and may not be applicable to every axis (for example, a swivel axis centerline can be below table surface). Essentially analogous schemes using the ball bar have been presented in [22], which requires one of the spheres of the ball bar nominally on the rotary axis. Clearly, these methods are not suitable for periodic accuracy inspection.

A critical issue with probing-based error identification methods is that it requires either 1) an artefact of the pre-calibrated geometry, or 2) axes, not under the test, of the pre-calibrated error motions. For periodic check of machine

tool geometric errors, it does not make sense to assume negligibly small linear axis error motions. Thermal influence, or long-term change in the ground or guideway, likely changes linear axis error motions.

To address this issue, Zimmermann and Ibaraki [23] applied a self-calibration technique to separate linear axis geometric errors from rotary axis geometric errors for the probing tests with an uncalibrated test piece. For the circularity measurement, to separate the geometric error of the measured test piece and the radial error motion of rotary table, self-calibration schemes have been well developed [24]. They can be classified into the Donaldson reversal, multi-step and multi-probe methods [25]. Although the method presented in [16] is essentially the multi-step method, it focuses on the separation of rotary and linear axis error motions, with using an uncalibrated nominally-cylindrical test piece. Only the linear positioning error of a single linear axis must be directly measured by probing an artefact of the precalibrated length. All the other error motions can be estimated by the present self-calibration scheme. It is not possible for any self-calibration schemes to estimate "the absolute" size of the test piece when the machine's positioning error is completely unknown. This is also true for well-established self-calibration schemes for the circularity measurement. Any self-calibration schemes, as reviewed in [23], can estimate the roundness profile of the test piece, i.e. the variation of the contour profile from the best-fit circle, under the influence of the radial error motion of the rotary table. However, none of them can estimate the mean diameter, when the displacement sensor positions are unknown.

Based on our preliminary work [23], original contributions of this paper are summarized in Table 1: 1) Zimmermann and Ibaraki [23] only presented an algorithm to identify the C-axis radial error motion and the positioning error of X- and Y-axis, by performing the proposed self-calibration test at $B = 0^\circ$ (with the table horizontal). This paper extends it to the identification of the axial error motion of C-axis and 3D error motions of linear axes. Furthermore, by performing the analogous test at $B = -90^\circ$ and $B = 90^\circ$ (with the table vertical), the C-axis error motions, as well as linear axis error motions, are identified

over the entire workspace. 2) Two case studies are presented to demonstrate the applicability of the proposed test to periodic machine tool accuracy check without using a pre-calibrated artefact. In the first case study, the proposed tests were periodically performed on the same five-axis machine tool for half a year to observe a long-term change in linear and rotary axis geometric errors. The second case study investigated the influence of room temperature change on linear and rotary axis error motions. Performance of thermal compensation done by a commercial machine tool controller can be checked.

Table 1: Comparison of this paper and our previous work [23] in the identifiable geometric errors

		Previous work [23]	This paper
C-axis	Position error of axis average line, (E_{X0C}, E_{Y0C})	✓	✓
	Radial error motion, (E_{XC}, E_{YC})	✓	✓
	Axial error motion, E_{ZC}		✓
	Squareness error of C- to X- and Y-axis, (E_{A0C}, E_{B0C})		✓
B-axis	Position error of axis average line, (E_{X0B}, E_{Z0B})		✓
	Angular positioning error at B $= -90°, 0°, 90°$, E_{BB}		✓
	Squareness error of B- to X- and Z-axis, (E_{A0B}, E_{C0B})		✓
X-, Y-, and Z-axes	Position error in radial direction, $E_{\text{radial},XY}$	✓	✓
	Squarenes error of Y- to X-axis, $E_{C(0X)Y}$	✓	✓
	Straightness error motion in Z direction, (E_{ZX}, E_{ZY})		✓
	Squarenes error of Z- to Y-axis, $E_{A(0Y)Z}$		✓
Case studies presented		Comparison with the R-Test	1) Long-term monitoring over half a year, 2) Investigation of thermal influence of room temperature

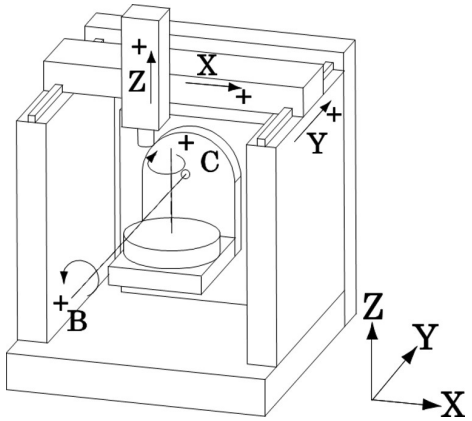

Figure 1: Configuration of the machine tool

2. Objective and the proposed test procedure

2.1. Overview

This paper targets a five-axis machine of the configuration shown in Fig. 1. The proposed method needs a nominally cylindrical test piece whose exact geometry is not calibrated. The surface of its side and top surfaces to be probed should be sufficiently smooth such that the probing is not influenced by the surface finish.

As is reviewed in Section 1, many five-axis machine tool builders provide a probing-based scheme to identify, and then compensate for, rotary axis geometric errors. Fig. 2(a) depicts a typical setup. A machine tool user places a precision sphere on the machine rotary table. A touch-trigger probe measures the position of its center in a semi-automated manner. As the sphere is indexed at a given set of rotary axis angles, the sphere position is probed. As an illustrative example, Fig. 2(b) shows the influence of the position error of the C-axis average line on the probed positions of the sphere. In the coordinate system with its origin at the nominal C-axis position, the trajectory of the probed sphere positions becomes a circle with its center offset equal to the C-axis position error.

It is important to note that this calculation assumes that linear axes have negligibly small error motions. A touch-trigger probe measures the relative displacement of the spindle to the work table. Therefore, all the axes involved, C-, X- and Y-axes in the example shown in Fig. 2, influence the probed positions. When linear axes have significant error motions, the measured trajectory in Fig. 2(b) can show significant circularity error, which subsequently causes an error in the identified rotary axis geometric errors.

To separately identify rotary and linear axis geometric errors, this paper proposes a self-calibration scheme. The presented measurement schemes are composed of Step S and Step T, probing the side face and the top face of the test piece, respectively.

2.2. Error variables to be identified

The objective of the proposed tests (Tests S and T), to be presented in Section 3, is to identify all the error variables defined in Tables 2 to 5.

Each variable is defined for a given set of C_i or θ_i. C_i represents the angular position of C-axis, and θ_i represents the angular position of the probed point on the test piece. C_i is defined positive clockwise, according to typical machine tool sign convention, but θ_i is defined positive counter-clockwise. In the example test procedure in Section 3, C_i or θ_i are given by $C_i, \theta_i = 0°, 45°, ..., 315°(i = 1, 2, ..., 8)$. Therefore, Tables 2 to 5 respectively contain a total of 32, 28, 26 and 18 parameters. In this paper, the machine coordinate system (MCS) represents the fixed coordinate system with its origin at the nominal intersection of B- and C-axes. The error symbols in Table 2, such as E_{XC}, E_{YC}, E_{X0C}, and E_{Y0C}, are defined in ISO 230-1 [26].

Tables 2 and 3 show the error parameters to be identified by probing the side face of the test piece (Tests S) at B = 0° (in Table 2) and B = −90° and B = 90° (in Table 3). In Table 3, $E_{ZC,\text{total}}$ at B = ±90° contains E_{Z0C} at B = ±90°, which represents the position error of the C-axis average line from its nominal position at B = ±90°. The nominal Z position of C-axis at B = ±90° is defined at the Z-position of B-axis. Therefore, it contains the position error of the B-axis average line, E_{Z0B}. According to the kinematic model in [11], when the B-axis average line has the position error in X and Z directions, E_{X0B} and E_{Z0B}, the C-axis position error at B = 0°, denoted by $(E_{X0C}(0°), E_{Y0C}(0°))$, is related to the C-axis position error at B = −90°, $(E_{X0C}(-90°), E_{Y0C}(-90°))$, by:

$$\begin{cases} E_{Y0C}(-90°) = E_{Y0C}(0°) \\ E_{Z0C}(-90°) = E_{X0C}(0°) - E_{X0B} - E_{Z0B} \end{cases} \tag{1}$$

Furthermore, the radial error motion of C-axis, (E_{XC}, E_{YC}), may vary at B = ±90° due to, for example, the elastic deformation of the C-axis bearing caused by the gravity influence. This is why $(E_{YC,\text{total}}, E_{ZC,\text{total}})$ at B = ±90° is defined separately in Table 3 from $(E_{XC,\text{total}}, E_{YC,\text{total}})$ at B = 0° in Ta-

ble 2. Similarly, due to, for example, the angular positioning error of B-axis and the tilt error motion of B-axis, the C-axis average line at $\mathrm{B} = 0^\circ$ and $\mathrm{B} = \pm 90^\circ$ may not be perfectly perpendicular to each other. This is why $(E_{C(0Y)C,\pm 90^\circ}, E_{B(0Z)C,\pm 90^\circ})$ at $\mathrm{B} = \pm 90^\circ$ is defined separately in Table 5 from $(E_{A(0Y)C,0^\circ}, E_{B(0X)C,0^\circ})$ at $\mathrm{B} = 0^\circ$ in Table 4. Note that the test piece's geometry, $W_{\mathrm{radial}}(\theta_i)$, is already identified at $\mathrm{B} = 0^\circ$ (Table 2), and thus is not included in Table 3. However, the test piece may be displaced at $\mathrm{B} = \pm 90^\circ$ due to, for example, the position error of B-axis average line. This displacement is represented by $(w_{Y,\pm 90^\circ}, w_{Z,\pm 90^\circ})$, which is to be identified.

When the test piece's top face is probed at $\mathrm{B} = 0^\circ$ (Tests T), Table 4 similarly shows the error variables. According to ISO 230-1 [26], the axial error motion of C-axis represents its position error in the direction of its axis average line, and thus the squareness error of the C-axis average line to X- and Y-axes, $E_{A(0Y)C,0^\circ}$ and $E_{B(0X)C,0^\circ}$, must be identified separately. Table 5 similarly shows the error variables identified by probing the test piece's top face at $\mathrm{B} = -90^\circ$ and $\mathrm{B} = 90^\circ$.

The uncertainty analysis for the error variables to be identified in Table 2 was presented in our previous work [23]. The propagation of the uncertainty in the probing to each estimated variable was assessed by applying the Monte Carlo simulation. The same analysis can be applied to assess the uncertainty in all the error variables in Tables 3 to 5.

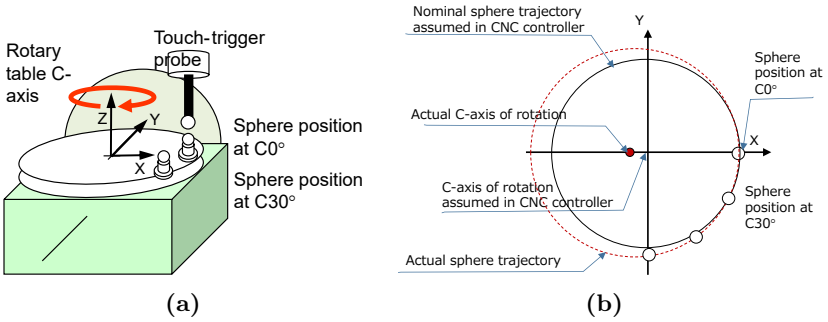

Figure 2: Principle in conventional probing-based identification schemes of rotary axis geometric error. (a) Typical test setup. (b) illustrative example: influence of the position error of the C-axis average line on the probed positions of the sphere.

Table 2: Error variables to be identified by Test S at B = 0°

Variable	Description
$E_{XC,\text{total}}(C_i, 0°)$	Displacement of C-axis in the X-direction when C-axis is indexed at C_i. It is given by the superposition of the X position error of the C-axis average line, E_{X0C}, and the radial error motion, E_{XC}, in the X direction as a function of the rotation angle C_i: $E_{XC,\text{total}}(C_i, 0°) = E_{X0C} + E_{XC}(C_i, 0°)$
$E_{YC,\text{total}}(C_i, 0°)$	Displacement of C-axis in the Y-direction when C-axis is indexed at C_i. Similarly it is given by the superposition of the Y position error of the C-axis average line, E_{Y0C}, and the radial error motion, E_{YC}, in the Y direction.
$E_{\text{radial},XY}(\theta_i, 0°)$	Positioning error of X- and Y-axes in the radial direction of the test piece, when X- and Y-axes are positioned at $(R{\cdot}\cos\theta_i, R{\cdot}\sin\theta_i)$. R represents the nominal radius of the test piece. It is given by the superposition of various error motions of X- and Y-axis, such as the linear positioning and straightness error motions, and the squareness error between X- and Y-axes.
$W_{\text{radial}}(\theta_i)$	Geometric profile of the test piece side surface in the radial direction at the angular position θ_i. It is defined in the MCS and thus includes the the setup position error of the test piece with respect to the origin of the MCS.

Table 3: Error variables to be identified by Test S at B = ±90°

Variable	Description
$E_{YC,\text{total}}(C_i, \pm 90^\circ)$	Displacement of C-axis in the Y-direction when C-axis is indexed at C_i. It is defined similarly as the one at B = 0° (in Table 2), but it contains the C-axis position and radial error motion at B = ±90°: $E_{YC,\text{total}}(C_i, \pm 90^\circ) = E_{Y0C} + E_{YC}(C_i, \pm 90^\circ)$
$E_{ZC,\text{total}}(C_i, \pm 90^\circ)$	Displacement of C-axis in the Z-direction when C-axis is indexed at C_i. Similarly it is given by the superposition of the Z position error of the C-axis average line, E_{Z0C}, and the radial error motion, E_{ZC}, in the Z direction.
$E_{\text{radial},YZ}(\theta_i, \pm 90^\circ)$	Positioning error of Y- and Z-axes in the radial direction of the test piece, when Y- and Z-axes are positioned at $(R \cdot \cos\theta_i, R \cdot \sin\theta_i)$.
$w_{Y,\pm 90^\circ}$	Displacement of the test piece center position in the Y direction at B = ±90° in the MCS.
$w_{Z,\pm 90^\circ}$	Displacement of the test piece center position in the Z direction at B = ±90° in the MCS.

Table 4: Error variables to be identified by Test T at B = 0°

Variable	Description
$E_{ZC}(C_i, 0°)$	Axial error motion of C-axis at B = 0° in the Z direction as a function of the rotation angle C_i.
$E_{ZZ}(\theta_i, 0°)$	Positioning error of linear axes in the Z(axial) direction, when positioned at $(X, Y) = (R \cdot \cos\theta_i, R \cdot \sin\theta_i)$. It may contain all the error motions of X, Y and Z-axes but the straightness error motion of X- and Y-axes in the Z-direction is typically a dominant contributor.
$W_{\text{axial}}(\theta_i)$	Geometric profile of the test piece top surface in the axial direction, at $(X, Y) = (R \cdot \cos\theta_i, R \cdot \sin\theta_i)$. It is defined in the MCS and thus it contains not only the flatness profile of the test piece, but also its orientation with respect to the machine's XY plane.
$E_{A(0Y)C,0°}$	Squareness between the Y-axis and C-axis at B = 0°, defined positive counter-clockwise from the positive X-direction.
$E_{B(0X)C,0°}$	Squareness between the X-axis and C-axis at B = 0°, defined positive counter-clockwise from the positive Y-direction.

Table 5: Error variables to be identified by Test T at B = ±90°

Variable	Description
$E_{XC}(C_i, \pm 90^\circ)$	Axial error motion of C-axis at B = −90° or B = 90° in the X direction as a function of the rotation angle C_i.
$E_{XX}(\theta_i, \pm 90^\circ)$	Positioning error of linear axes in the X(axial) direction, when positioned at $(Y, Z) = (R \cdot \cos\theta_i, R \cdot \sin\theta_i)$.
$E_{C(0Y)C,\pm 90^\circ}$	Squareness between the Y-axis and C-axis at B = ±90°, defined positive counter-clockwise from the positive Z-direction.
$E_{B(0Z)C,\pm 90^\circ}$	Squareness between the Z-axis and C-axis at B = ±90°, defined positive counter-clockwise from the positive Y-direction.

3. Proposed test procedure

The angular increment of C_i and θ_i should be designed according to the geometric accuracy of the machine and the test piece. This section presents the proposed test procedure with the angular increment 45°, i.e. $C_i, \theta_i = 0^\circ, 45^\circ, ..., 315^\circ$, but it is merely an example.

When the proposed tests, Tests S and T at B = 0°, ±90° (Figs. 3-6), are performed, the machine tool is assumed to be in a thermally stable condition. The total test time depends on various measurement conditions, for example, the probing feed rate, the standoff distance, and the rapid traverse speed between the probed points. In a set of the proposed tests, Tests S and T at B = 0°, ±90° (Figs. 3-6), total 192 points are probed. Typical test time is estimated 30 min approximately.

3.1. Step1: Probing side face of test piece

3.1.1. Tests S at B = 0°

Figure 3 illustrates the proposed test procedure at B = 0°.

1) In Test 1-a-S and 1-b-S, C-axis is indexed clockwise from 0° to 315° by increments of 45°. The point on the test piece's cylindrical face located at 0° (in

Test 1-a-S) and 45° (in Test 1-b-S) is probed. Since the probing is normally always at the same (X, Y) position, Test 1-a-S and 1-b-S can exclude the influence of $E_{\mathrm{radial},XY}(\theta_i, 0°)$.

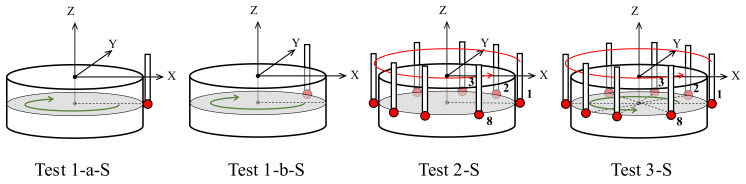

Figure 3: Proposed measurement procedure, Tests S at B = 0° (1-a-S, 1-b-S, 2-S, 3-S)

2) In Test 2-S, C-axis is fixed and the target points are probed, located at every 45° from 0° to 315°, by positioning by X- and Y-axes. Since C-axis does not rotate, Test 2-S can exclude the influence of $E_{XC,\mathrm{total}}(C_i, 0°)$ and $E_{YC,\mathrm{total}}(C_i, 0°)$.

3) In Test 3-S, C-axis is indexed at every 45° from 0° to 315°, and X- and Y-axes are positioned such that the same point on the side face of test piece is probed at every C angle. Test 3-S can exclude the influence of $W_{radial}(\theta_i)$.

3.1.2. Direct measurement of X-axis linear positioning error by probing the pre-calibrated bar

For the proposed self-calibration scheme, it is not possible to estimate "absolute" distance when neither of the machine linear axes and the test piece are calibrated. It is, in principle, the same with the self-calibration schemes for the circularity measurement [24]; it is not possible to estimate the diameter of the test piece by any self-calibration schemes. In the proposed test procedure, only the linear positioning error of X-axis is directly measured by using a calibrated bar artefact. This is only error that cannot be estimated by the proposed self-calibration scheme.

As an artefact, a ceramic bar ($20 \times 20 \times 300$ mm), whose length was pre-calibrated by a coordinate measuring machine, is used. The bar's is made of silicon nitride, and its coefficient of thermal expansion is 1.79×10^{-6} [m/K] at room temperature.

3.1.3. Tests S at B = ±90°

As shown in Fig. 4, similar tests are conducted at B = −90°. The test piece is probed in the YZ plane. The test procedure is analogous to the one presented in Section 3.1.1. Analogous tests are conducted also at B = 90° in the YZ plane.

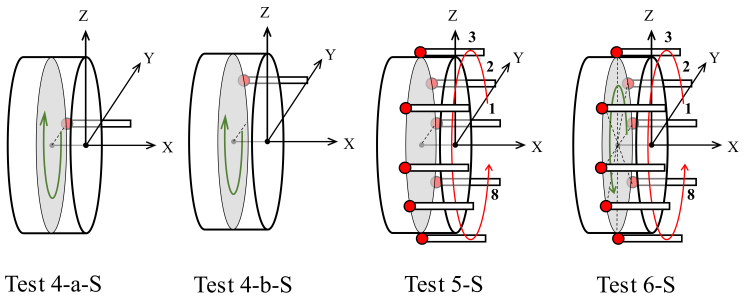

Figure 4: Proposed measurement procedure, Tests S at B = −90° (4-a-S, 4-b-S, 5-S, 6-S)

3.2. Step2: Probing top face of test piece

3.2.1. Tests T at B = 0°

Figure 5 illustrates the proposed test procedure at B = 0°.

1) In Test 1-a-T and 1-b-T, C-axis is indexed clockwise from 0° to 315° by increments of 45°. The point on the test piece's top face located at 0° (in Test 1-a-T) and 45° (in Test 1-b-T) is probed. Since the probing is normally always at the same (X, Y) position, Test 1-a-T and 1-b-T can exclude the influence of $E_{ZZ}(\theta_i, 0°)$, $E_{A(0Y)C,0°}$, and $E_{B(0X)C,0°}$.

2) In Test 2-T, C-axis is fixed and the target points are probed, located at every 45° from 0° to 315°, by positioning by X- and Y-axes. Since C-axis does not rotate, Test 2-T can exclude the influence of $E_{ZC}(C_i, 0°)$.

3) In Test 3-T, C-axis is indexed at every 45° from 0° to 315°, and the same point on the top face of the test piece is probed at every C angle. Test 3-T can exclude the influence of $W_{\text{axial}}(\theta_i)$.

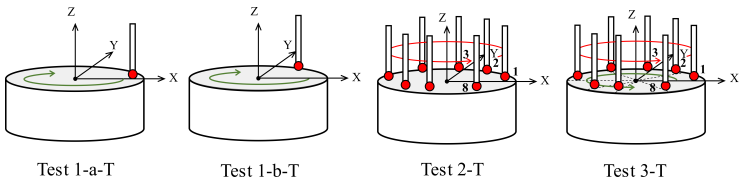

Figure 5: Proposed measurement procedure, Tests T at B = 0° (1-a-T, 1-b-T, 2-T, 3-T)

3.2.2. Tests T at B = ±90°

Figure 6 illustrates the measurement procedure at B = −90°. Test procudure is analogous to the one in Section 3.2.1 except for that the target point's displacement in the X-direction is probed. Analogous tests are conducted also at B = 90°.

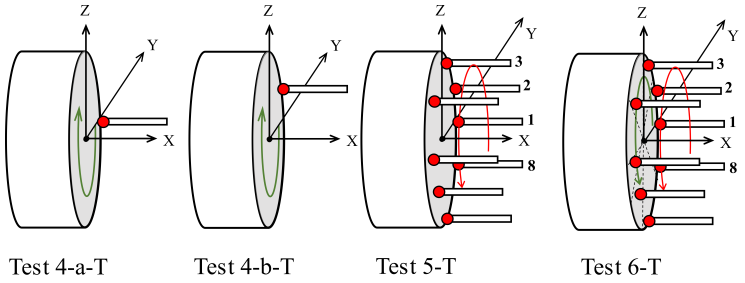

Figure 6: Proposed measurement procedure, Tests T at B = −90° (4-a-T, 4-b-T, 5-T, 6-T)

4. Algorithm to identify the error variables

4.1. Step1: Probing side face of test piece

4.1.1. Tests S at B = 0°

A touch-trigger probe is sensitive only to the target point's position in the direction normal to the surface. Therefore, for Tests S at B = 0°, when the C-axis angular position is C_i, and the touch-trigger probe is positioned at $(R \cdot \cos\theta_i, R \cdot \sin\theta_i)$, the distance of the probed point to the MCS origin, denoted by $r(C_i, \theta_i)$, is measured. Then, its change from the initial measurement at

250 $C_i = \theta_i = 0^\circ$ is taken as the inputs to the proposed algorithm:

$$\Delta r(C_i, \theta_i) = r(C_i, \theta_i) - r(0^\circ, 0^\circ) \tag{2}$$

Test 1-a-S (see Fig. 3) is formulated as an example. 1) When C-axis is indexed at C_i, the C-axis centerline is displaced by $(E_{XC,\mathrm{total}}(C_i, 0^\circ), E_{YC,\mathrm{total}}(C_i, 0^\circ))$. Since a unit vector representing the probe's sensitive direction is $(\cos 0^\circ, \sin 0^\circ)$ (in Test 1-a-S, this is always the probing direction in the MCS), its influence on the measured radial displacement is represented by the inner product of $(E_{XC,\mathrm{total}}(C_i, 0^\circ), E_{YC,\mathrm{total}}(C_i, 0^\circ))$ and $(\cos 0^\circ, \sin 0^\circ)$. 2) When the C-axis is at C_i, the probe touches the point on the test piece at θ_i. Thus, the test piece's geometric error in the radial direction at θ_i, denoted by $W_{\mathrm{radial}}(\theta_i)$, directly affects the probed displacement. 3) The positioning error of X- and Y-axes does not influence since X- and Y-positions are nominally always the same. Adding 1) to 3), the measured radial displacement at C_i in Test 1-a-S is formulated by:

$$\Delta r_{1-\mathrm{a}-\mathrm{S}}(C_i) = \begin{bmatrix} E_{XC,\mathrm{total}}(C_i, 0^\circ) \\ E_{YC,\mathrm{total}}(C_i, 0^\circ) \end{bmatrix} \cdot \begin{bmatrix} \cos 0^\circ \\ \sin 0^\circ \end{bmatrix} + W_{\mathrm{radial}}(C_i) \tag{3}$$

Similarly, the measured radial displacements in Tests 1-b-S, 2-S, and 3-S are written by:

$$\Delta r_{1-\mathrm{b}-\mathrm{S}}(C_i) = \begin{bmatrix} E_{XC,\mathrm{total}}(C_i, 0^\circ) \\ E_{YC,\mathrm{total}}(C_i, 0^\circ) \end{bmatrix} \cdot \begin{bmatrix} \cos 45^\circ \\ \sin 45^\circ \end{bmatrix} - E_{\mathrm{radial},XY}(45^\circ, 0^\circ) + W_{\mathrm{radial}}(C_i + 45^\circ) \tag{4}$$

$$\Delta r_{2-\mathrm{S}}(\theta_i) = -E_{\mathrm{radial},XY}(\theta_i, 0^\circ) + W_{\mathrm{radial}}(\theta_i) \tag{5}$$

$$\Delta r_{3-\mathrm{S}}(C_i, \theta_i) = \begin{bmatrix} E_{XC,\mathrm{total}}(-C_i, 0^\circ) \\ E_{YC,\mathrm{total}}(-C_i, 0^\circ) \end{bmatrix} \cdot \begin{bmatrix} \cos C_i \\ \sin C_i \end{bmatrix} - E_{\mathrm{radial},XY}(\theta_i, 0^\circ) \tag{6}$$

As is mentioned in Section 3.1.1, each test does not contain one of the error sources ($E_{X/YC,\mathrm{total}}(C_i, 0°)$, $W_{\mathrm{radial}}(\theta_i)$, and $E_{\mathrm{radial},XY}(\theta_i, 0°)$). Eqs. (3)–(6) can be combined in a matrix form:

$$\begin{bmatrix} \Delta r_{1-\mathrm{a-S}}(C_1) \\ \Delta r_{1-\mathrm{b-S}}(C_1) \\ \Delta r_{2-\mathrm{S}}(\theta_1) \\ \Delta r_{3-\mathrm{S}}(C_1, \theta_1) \\ \vdots \\ \Delta r_{1-\mathrm{a-S}}(C_8) \\ \Delta r_{1-\mathrm{b-S}}(C_8) \\ \Delta r_{2-\mathrm{S}}(\theta_8) \\ \Delta r_{3-\mathrm{S}}(C_8, \theta_8) \end{bmatrix} = \boldsymbol{A}_{\mathbf{radial,B0}} \cdot \begin{bmatrix} E_{XC,\mathrm{total}}(C_1, 0°) \\ E_{YC,\mathrm{total}}(C_1, 0°) \\ E_{\mathrm{radial},XY}(\theta_1, 0°) \\ W_{\mathrm{radial}}(\theta_1) \\ \vdots \\ E_{XC,\mathrm{total}}(C_8, 0°) \\ E_{YC,\mathrm{total}}(C_8, 0°) \\ E_{\mathrm{radial},XY}(\theta_8, 0°) \\ W_{\mathrm{radial}}(\theta_8) \end{bmatrix} \tag{7}$$

where $\boldsymbol{A}_{\mathbf{radial,B0}}$ matrix has the size of 32×32. However, $\boldsymbol{A}_{\mathbf{radial,B0}}$ has rank deficiency. The following boundary conditions have to be imposed to solve Eq. (7) using the least squares method. Firstly, the following four boundary conditions are required because $\Delta r(C_i, \theta_i)$ is defined relative to $\Delta r(0°, 0°)$.

$$\begin{cases} E_{XC,\mathrm{total}}(0°, 0°) = 0 \\ E_{YC,\mathrm{total}}(0°, 0°) = 0 \\ E_{\mathrm{radial},XY}(0°, 0°) = 0 \\ W_{\mathrm{radial}}(0°) = 0 \end{cases} \tag{8}$$

The C-axis error motions, $(E_{XC,\mathrm{total}}, E_{YC,\mathrm{total}})$, and the geometric profile of the test piece side surface, W_{radial}, are defined with respect to the MCS. The origin of the MCS is defined based on the positioning by linear axes. The following constraints are needed to define the MCS origin:

$$\begin{cases} E_{\mathrm{radial},XY}(90°, 0°) = 0 \\ E_{\mathrm{radial},XY}(180°, 0°) = \Delta L \end{cases} \tag{9}$$

The need for these constraints can be understood as follows: If the MCS

origin, the C-axis centerline, and the test piece, are all moved by the same distance to Y-direction, it clearly does not influence the probed displacements at all. The first constraint in Eq. (9) is needed to avoid this redundancy. The second constraint in Eq. (9) is needed since the "absolute" distance cannot be estimated by any self-calibration schemes, as was discussed in Section 1. With six constraints imposed, $\boldsymbol{A}_{\mathbf{radial,B0}}$ has the size of 32×26, and becomes full rank. As a result, 26 unknown variables can be identified by solving Eq. (7).

4.1.2. Tests S at $\mathrm{B} = \pm 90^\circ$

The formulations of for Tests S at $\mathrm{B} = -90^\circ$ and $\mathrm{B} = 90^\circ$ are essentially the same as Eqs. (3)–(6). A difference is that the geometric error of the test piece, $W_{\mathrm{radial}}(\theta_i)$, is identified at $\mathrm{B} = 0^\circ$ and thus is considered as known variables at $\mathrm{B} = \pm 90^\circ$. Only the displacements of the test piece center, $w_{Y,\pm 90^\circ}$, $w_{Z,\pm 90^\circ}$, in Table 3 must be identified. For $\mathrm{B} = -90^\circ$, the probed displacements in Tests 4-a-S, 4-b-S, 5-S, and 6-S are respectively formulated as follows:

$$\Delta r_{4-\mathrm{a}-\mathrm{S}}(C_i) = \begin{bmatrix} E_{YC,\mathrm{total}}(C_i, -90^\circ) \\ E_{ZC,\mathrm{total}}(C_i, -90^\circ) \end{bmatrix} \cdot \begin{bmatrix} \cos 0^\circ \\ \sin 0^\circ \end{bmatrix} + W_{\mathrm{radial}}(C_i + 90^\circ) - W_{\mathrm{radial}}(90^\circ) + \begin{bmatrix} w_{Y,-90^\circ} \\ w_{Z,-90^\circ} \end{bmatrix} \cdot \begin{bmatrix} \cos C_i - 1 \\ \sin C_i \end{bmatrix} \quad (10)$$

$$\Delta r_{4-\mathrm{b}-\mathrm{S}}(C_i) = \begin{bmatrix} E_{YC,\mathrm{total}}(C_i, -90^\circ) \\ E_{ZC,\mathrm{total}}(C_i, -90^\circ) \end{bmatrix} \cdot \begin{bmatrix} \cos 45^\circ \\ \sin 45^\circ \end{bmatrix} - E_{\mathrm{radial},YZ}(45^\circ, -90^\circ) + W_{\mathrm{radial}}(C_i + 135^\circ) - W_{\mathrm{radial}}(90^\circ) + \begin{bmatrix} w_{Y,-90^\circ} \\ w_{Z,-90^\circ} \end{bmatrix} \cdot \begin{bmatrix} \cos(C_i + 45^\circ) - 1 \\ \sin(C_i + 45^\circ) \end{bmatrix} \quad (11)$$

$$\Delta r_{5-\mathrm{S}}(\theta_i) = -E_{\mathrm{radial},YZ}(\theta_i, -90^\circ) + W_{\mathrm{radial}}(\theta_i + 90^\circ) - W_{\mathrm{radial}}(90^\circ) + \begin{bmatrix} w_{Y,-90^\circ} \\ w_{Z,-90^\circ} \end{bmatrix} \cdot \begin{bmatrix} \cos\theta_i - 1 \\ \sin\theta_i \end{bmatrix} \quad (12)$$

$$\Delta r_{6-\mathrm{S}}(C_i, \theta_i) = \begin{bmatrix} E_{YC,\mathrm{total}}(-C_i, -90^\circ) \\ E_{ZC,\mathrm{total}}(-C_i, -90^\circ) \end{bmatrix} \cdot \begin{bmatrix} \cos C_i \\ \sin C_i \end{bmatrix} - E_{\mathrm{radial},YZ}(\theta_i, -90^\circ) \quad (13)$$

Eqs. (10)–(13) can be expressed by:

$$\begin{bmatrix} \Delta r_{4-\mathrm{a}-\mathrm{S}}(C_1) \\ \Delta r_{4-\mathrm{b}-\mathrm{S}}(C_1) \\ \Delta r_{5-\mathrm{S}}(\theta_1) \\ \Delta r_{6-\mathrm{S}}(C_1, \theta_1) \\ \vdots \\ \Delta r_{4-\mathrm{a}-\mathrm{S}}(C_8) \\ \Delta r_{4-\mathrm{b}-\mathrm{S}}(C_8) \\ \Delta r_{5-\mathrm{S}}(\theta_8) \\ \Delta r_{6-\mathrm{S}}(C_8, \theta_8) \end{bmatrix} = \boldsymbol{A}_{\mathbf{radial,B-90}} \cdot \begin{bmatrix} E_{YC,\mathrm{total}}(C_1, -90^\circ) \\ E_{ZC,\mathrm{total}}(C_1, -90^\circ) \\ E_{\mathrm{radial},YZ}(\theta_1, -90^\circ) \\ \vdots \\ E_{YC,\mathrm{total}}(C_8, -90^\circ) \\ E_{ZC,\mathrm{total}}(C_8, -90^\circ) \\ E_{\mathrm{radial},YZ}(\theta_8, -90^\circ) \\ w_{Y,-90^\circ} \\ w_{Z,-90^\circ} \end{bmatrix} \quad (14)$$

Similarly as in $\mathrm{B} = 0^\circ$, the following boundary conditions should be imposed:

$$\begin{cases} E_{YC,\mathrm{total}}(0^\circ, -90^\circ) = 0 \\ E_{ZC,\mathrm{total}}(0^\circ, -90^\circ) = 0 \\ E_{\mathrm{radial},YZ}(0^\circ, -90^\circ) = 0 \end{cases} \quad (15)$$

$$\begin{cases} E_{\mathrm{radial},YZ}(90^\circ, -90^\circ) = 0 \\ E_{\mathrm{radial},YZ}(180^\circ, -90^\circ) = E_{\mathrm{radial},XY}(270^\circ, 0^\circ) \end{cases} \quad (16)$$

4.2. Step2: Probing top face of test piece

4.2.1. Tests T at $\mathrm{B} = 0^\circ$

When the C-axis angular position is C_i and the touch-trigger probe is positioned at $(R\cdot\cos\theta_i, R\cdot\sin\theta_i)$, denote the displacement of the probed point in the Z-direction by $h(C_i, \theta_i)$. Its displacement from the initial position, $\Delta h(C_i, \theta_i)$, is defined as:

$$\Delta h(C_i, \theta_i) = h(C_i, \theta_i) - h(0^\circ, 0^\circ) \tag{17}$$

Thus, the Test 1-a-T, 1-b-T, 2-T, and 3-T, shown in Fig. 5, can be expressed as Eqs. (18)–(21), respectively.

$$\Delta h_{1-\mathrm{a}-\mathrm{T}}(C_i) = E_{ZC}(C_i, 0^\circ) + W_{\mathrm{axial}}(C_i) \tag{18}$$

$$\begin{aligned}\Delta h_{1-\mathrm{b}-\mathrm{T}}(C_i) = {} & E_{ZC}(C_i, 0^\circ) - E_{ZZ}(45^\circ, 0^\circ) + W_{\mathrm{axial}}(C_i + 45^\circ) \\ & + \begin{bmatrix} E_{A(0Y)C,0^\circ} \\ E_{B(0X)C,0^\circ} \end{bmatrix} \cdot \begin{bmatrix} R\cdot\sin 45^\circ \\ R\cdot(1-\cos 45^\circ) \end{bmatrix}\end{aligned} \tag{19}$$

$$\begin{aligned}\Delta h_{2-\mathrm{T}}(\theta_i) = {} & -E_{ZZ}(\theta_i, 0^\circ) + W_{\mathrm{axial}}(\theta_i) \\ & + \begin{bmatrix} E_{A(0Y)C,0^\circ} \\ E_{B(0X)C,0^\circ} \end{bmatrix} \cdot \begin{bmatrix} R\cdot\sin\theta_i \\ R\cdot(1-\cos\theta_i) \end{bmatrix}\end{aligned} \tag{20}$$

$$\begin{aligned}\Delta h_{3-\mathrm{T}}(C_i, \theta_i) = {} & E_{ZC}(-C_i, 0^\circ) - E_{ZZ}(\theta_i, 0^\circ) \\ & + \begin{bmatrix} E_{A(0Y)C,0^\circ} \\ E_{B(0X)C,0^\circ} \end{bmatrix} \cdot \begin{bmatrix} R\cdot\sin C_i \\ R\cdot(1-\cos C_i) \end{bmatrix}\end{aligned} \tag{21}$$

Eqs. (18)–(21) can be combined in a matrix form:

$$\begin{bmatrix} \Delta r_{1-\mathrm{a}-\mathrm{T}}(C_1) \\ \Delta r_{1-\mathrm{b}-\mathrm{T}}(C_1) \\ \Delta r_{2-\mathrm{T}}(\theta_1) \\ \Delta r_{3-\mathrm{T}}(C_1, \theta_1) \\ \vdots \\ \Delta r_{1-\mathrm{a}-\mathrm{T}}(C_8) \\ \Delta r_{1-\mathrm{b}-\mathrm{T}}(C_8) \\ \Delta r_{2-\mathrm{T}}(\theta_8) \\ \Delta r_{3-\mathrm{T}}(C_8, \theta_8) \end{bmatrix} = \boldsymbol{A}_{\mathbf{axial,B0}} \cdot \begin{bmatrix} E_{ZC}(C_1, 0^\circ) \\ E_{ZZ}(\theta_1, 0^\circ) \\ W_{\mathrm{axial}}(\theta_1) \\ \vdots \\ E_{ZC}(C_8, 0^\circ) \\ E_{ZZ}(\theta_8, 0^\circ) \\ W_{\mathrm{axial}}(\theta_8) \\ E_{A(0Y)C,0^\circ} \\ E_{B(0X)C,0^\circ} \end{bmatrix} \tag{22}$$

Similarly as in tests S, the following boundary conditions should be imposed:

$$\begin{cases} E_{ZC}(0^\circ, 0^\circ) = 0 \\ E_{ZZ}(0^\circ, 0^\circ) = 0 \\ W_{\mathrm{axial}}(0^\circ) = 0 \end{cases} \tag{23}$$

The orientation of the XY plane of the MCS is defined parallel to the machine's XY plane. The following constraints, in addition to the second constraint in Eq. (23), define the orientation of the MCS:

$$\begin{cases} E_{ZZ}(90^\circ, 0^\circ) = 0 \\ E_{ZZ}(180^\circ, 0^\circ) = 0 \end{cases} \tag{24}$$

The following constraints are needed since the axial error motion of C-axis, $E_{ZC}(C_i, 0^\circ)$, is defined as the variation from the plane defined normal to the axis average line. In other words, the "mean" plane of $E_{ZC}(C_i, 0^\circ)$ must be parallel to the XY plane.

$$\begin{cases} E_{ZC}(90^\circ, 0^\circ) = 0 \\ E_{ZC}(180^\circ, 0^\circ) = 0 \end{cases} \tag{25}$$

4.2.2. Tests T at B $= \pm 90^\circ$

Similarly, for B $= -90^\circ$, the test 4-a-T, test4-b-T, test 5-T, and test 6-T, shown in Fig. 6, can be expressed as Eqs. (26)–(29), respectively.

$$\Delta h_{4-\mathrm{a}-\mathrm{T}}(C_i) \;=\; E_{XC}(C_i, -90^\circ) \,+\, W_{\mathrm{axial}}(C_i \,+\, 90^\circ) \,-\, W_{\mathrm{axial}}(90^\circ) \quad (26)$$

$$\begin{aligned}\Delta h_{4-\mathrm{b}-\mathrm{T}}(C_i) = {} & E_{XC}(C_i, -90^\circ) - E_{XX}(45^\circ, -90^\circ) \\ & + W_{\mathrm{axial}}(C_i + 135^\circ) - W_{\mathrm{axial}}(90^\circ) \\ & + \begin{bmatrix} E_{C(0Y)C,-90^\circ} \\ E_{B(0Z)C,-90^\circ} \end{bmatrix} \cdot \begin{bmatrix} R \cdot \sin 45^\circ \\ R \cdot (1 - \cos 45^\circ) \end{bmatrix}\end{aligned} \quad (27)$$

$$\begin{aligned}\Delta h_{5-\mathrm{T}}(\theta_i) = {} & -E_{XX}(\theta_i, -90^\circ) + W_{\mathrm{axial}}(\theta_i + 90^\circ) - W_{\mathrm{axial}}(90^\circ) \\ & + \begin{bmatrix} E_{C(0Y)C,-90^\circ} \\ E_{B(0Z)C,-90^\circ} \end{bmatrix} \cdot \begin{bmatrix} R \cdot \sin \theta_i \\ R \cdot (1 - \cos \theta_i) \end{bmatrix}\end{aligned} \quad (28)$$

$$\begin{aligned}\Delta h_{6-\mathrm{T}}(C_i, \theta_i) = {} & E_{XC}(-C_i, -90^\circ) - E_{XX}(\theta_i, -90^\circ) \\ & + \begin{bmatrix} E_{C(0Y)C,-90^\circ} \\ E_{B(0Z)C,-90^\circ} \end{bmatrix} \cdot \begin{bmatrix} R \cdot \sin(-C_i) \\ R \cdot (1 - \cos(-C_i)) \end{bmatrix}\end{aligned} \quad (29)$$

Eqs. (26)–(29) can be combined in a matrix form:

$$\begin{bmatrix} \Delta r_{4-\mathrm{a}-\mathrm{T}}(C_1) \\ \Delta r_{4-\mathrm{b}-\mathrm{T}}(C_1) \\ \Delta r_{5-\mathrm{T}}(\theta_1) \\ \Delta r_{6-\mathrm{T}}(C_1,\theta_1) \\ \vdots \\ \Delta r_{4-\mathrm{a}-\mathrm{T}}(C_8) \\ \Delta r_{4-\mathrm{b}-\mathrm{T}}(C_8) \\ \Delta r_{5-\mathrm{T}}(\theta_8) \\ \Delta r_{6-\mathrm{T}}(C_8,\theta_8) \end{bmatrix} = \boldsymbol{A}_{\mathbf{axial,B-90}} \cdot \begin{bmatrix} E_{XC}(C_1,-90^\circ) \\ E_{XX}(\theta_1,-90^\circ) \\ \vdots \\ E_{XC}(C_8,-90^\circ) \\ E_{XX}(\theta_8,-90^\circ) \\ E_{C(0Y)C,-90^\circ} \\ E_{B(0Z)C,-90^\circ} \end{bmatrix} \tag{30}$$

Similarly as in $\mathrm{B} = 0^\circ$, the following boundary conditions should be imposed:

$$\begin{cases} E_{XC}(0^\circ,-90^\circ) = 0 \\ E_{XC}(90^\circ,-90^\circ) = 0 \\ E_{XC}(180^\circ,-90^\circ) = 0 \\ E_{XX}(0^\circ,-90^\circ) = 0 \\ E_{XX}(90^\circ,-90^\circ) = 0 \\ E_{XX}(180^\circ,-90^\circ) = 0 \end{cases} \tag{31}$$

5. Case Study #1: Evaluation of long-term changes in rotary and linear axis geometric errors

5.1. Test objective

Geometric errors of linear and rotary axes in a five-axis machine tool change in a long term, due to, for example, environmental change. To demonstrate the application of the proposed scheme to long-term periodic monitoring of linear and rotary axis geometric errors, it was performed on the same five-axis machining center periodically over half a year.

5.2. Experimental setup

In experiments, a cylindrical test piece (approximate size: diameter 180 mm, height 50 mm, material: aluminum alloy, see Fig. 7) was measured on a vertical five-axis machining center, NMV3000 DCG by DMG Mori. Co., Ltd. Its configuration is shown in Fig. 1. According to ISO 10791-2 [27], the kinematic chain of the machine tool is expressed as follows: V[w-C-B-b-Y-X-Z-(C)-t]. Renishaw OMP400 touch-trigger probe was installed to the spindle (major specifications in the manufacturer's catalogue: Unidirectional repeatability (2σ): 0.35 μm for stylus length 100 mm, 3D pre-travel variation in X, Y, Z: $\pm$1.75 μm for stylus length 100 mm). The test piece was fixed on the table by two bolts. The cylindrical side surface of the test piece was rough-machined by a lathe but its geometry was not pre-calibrated. As shown in Fig. 7,"star styli" with three stylus spheres in vertical and horizontal directions were used to perform the proposed tests at B = 0°, B = −90°, and B = 90°. The nominal stylus lengths are shown in Fig. 7(a) and the actual lengths were precalibrated. The diameter of the stylus spheres was 6 mm. The actual probing repeatability depends also on the repeatability in the machine tool's positioning. The probing repeatability was investigated by experiments. For each stylus sphere, the same point was repeatedly probed for 20 times in X and Z directions. The measured unidirectional repeatability (in 2σ) was 0.00 μm in X direction, and 0.98 μm in Z direction, for the center stylus sphere. It was 1.02 μm in X direction, and 1.28 μm in Z

direction, for the left stylus sphere. It was verified that the probing repeatability error was not significantly larger than the machine tool's positioning resolution (and thus the probe's measurement resolution), 1 μm, for any of stylus spheres, in both horizontal (X) and vertical (Z) directions.

The same set of the tests was performed on July, September, December 2020 and January 2021. Table 6 shows the room temperature at each test. The machine tool is installed in a university laboratory, and is operated only occasionally over this half year for research purposes.

Table 6: Room temperature

Date	Jul./2020	Sep./2020	Dec./2020	Jan./2021
Room temperature [°C]	23.4	24.2	15.7	20.0

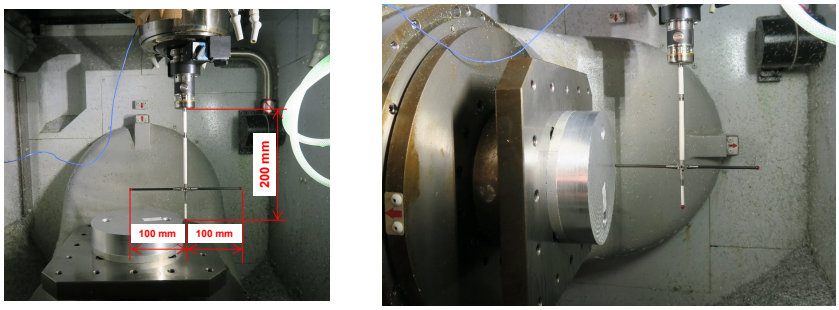

(a) **(b)**

Figure 7: Experimental setup (a) at B = 0° and (b) at B = −90°

5.3. Measurement result (Probing tests for side face with the table at horizontal position)

The expanded uncertainty (k=1) estimated by the measured unidirectional repeatability was 1.38 μm, which can be taken as standard uncertainty for the input quantities in the Monte Carlo method. To evaluate the uncertainties of the identified geometric errors, the Monte Carlo method with 1,000 runs was adopted to the self-calibration algorithm. The resulting expanded uncertainties (k=2) were presented in Figs. 9, 10, 12 and 13.

(1) Tests S at B = 0°

Tests 1-a-S to 3-S, depicted in Fig. 3, were performed at B = 0° (see Fig. 7(a)) to measure the radial displacement at each point, $\Delta r_{1-\mathrm{a}-\mathrm{S}}(C_i)$, $\Delta r_{1-\mathrm{b}-\mathrm{S}}(C_i)$, $\Delta r_{2-\mathrm{S}}(\theta_i)$, $\Delta r_{3-\mathrm{S}}(C_i, \theta_i)(i = 1, 2, ..., 8)$. Then, the algorithm presented in Section 4.1.1 was applied to identify all the error parameters in Table 2 (for $i = 1, 2, ..., 8$). To help intuitively understanding the identified errors, each error parameter is shown in Fig. 8 in a polar format.

(1-1) X-, Y-, and C-axis and test piece geometric errors identified by the proposed algorithm

Figure 8(a) shows the radial error motion of C-axis, $(E_{XC,\mathrm{total}}(C_i, 0^\circ), E_{YC,\mathrm{total}}(C_i, 0^\circ))$, identified by the four tests. If there exists no error, $(E_{XC,\mathrm{total}}(C_i, 0^\circ), E_{YC,\mathrm{total}}(C_i, 0^\circ))$ is at the origin. The center of the trajectory of $(E_{XC,\mathrm{total}}(C_i, 0^\circ), E_{YC,\mathrm{total}}(C_i, 0^\circ))$, shown by the cross mark in Fig. 8(a), represents the position error of the C-axis average line from its nominal position (E_{X0C}, E_{Y0C}). It can be observed that the C-axis position moved by 22 μm in X-direction, and 38 μm in Y-direction, during four tests over half a year. This is likely caused by thermal deformation of the machine structure. In Fig. 8(a), the mean radius of each trajectory significantly varies, which is directly caused by the C-axis position error, due to the boundary condition in Eq. (8). The radial deviation of the trajectory $(E_{XC,\mathrm{total}}(C_i, 0^\circ), E_{YC,\mathrm{total}}(C_i, 0^\circ))$ from its best-fit circle represents the radial error motion of C-axis; it is not significant in any tests in Fig. 8.

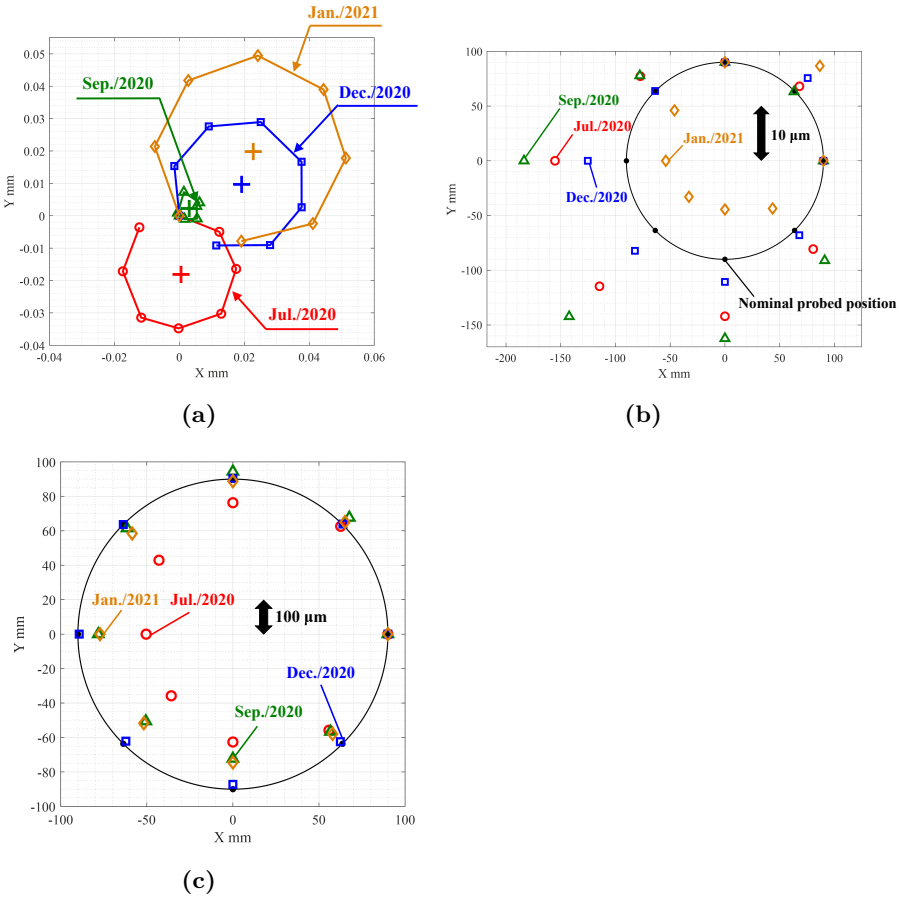

Figure 8: (a) Identified C-axis error motions at $\mathrm{B} = 0°$, $E_{XC,\mathrm{total}}(C_i, 0°)$ and $E_{YC,\mathrm{total}}(C_i, 0°)$ (b) Identified positioning error of X- and Y-axes in the radial direction, $E_{\mathrm{radial},XY}(\theta_i, 0°)$. The error from the nominal probed position is magnified 5,000 times. (c) Identified test piece geometric error, $W_{\mathrm{radial}}(\theta_i)$. The error from the nominal probed position is magnified 200 times.

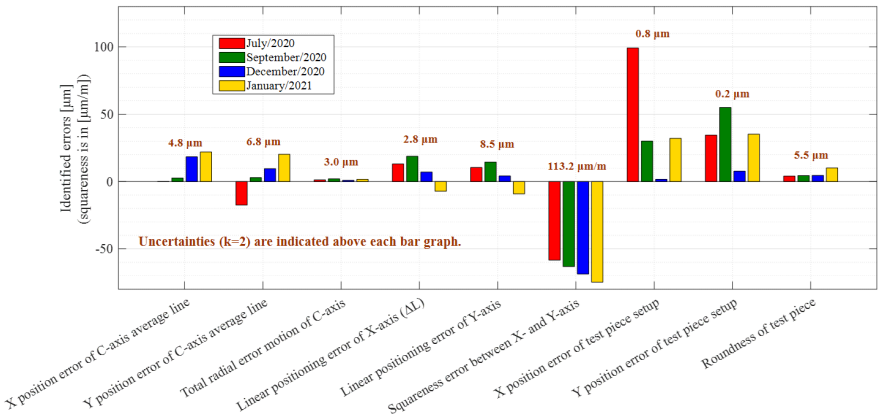

Figure 9: Geometric errors of rotary and linear axes and the test piece identified by Tests S at B = 0° (Red bar: Jul./2020, Green bar: Sep./2020, Blue bar: Dec./2020, Yellow bar: Jan./2021)

Fig. 8(b) shows the (X,Y) positioning error in the radial direction, $E_{\text{radial},XY}(\theta_i, 0°)$, identified by the four tests. The black circle represents zero error, $E_{\text{radial},XY}(\theta_i, 0°) = 0$, and the identified $E_{\text{radial},XY}(\theta_i, 0°)$, magnified 5,000 times, is plotted in the radial direction from the command point shown in a black dot. In other words, 50 mm in Fig. 8(b) is equivalent to 10 μm error. In Fig. 8(b), all trajectories are elliptical, with their axis tilted by 45° from the X-axis. Analogous to the circular test described in ISO 230-4 [28], this shows the influence of the squareness error between X- and Y-axis. Furthermore, Fig. 8(b) shows that the linear positioning error of the X-axis, represented by the identified error at $\theta_i = 180°$, varied approximately by 20 μm. Note that the identified errors at $\theta_i = 0°$ and 90° are are constrained to zero by Eqs. (8) and (9).

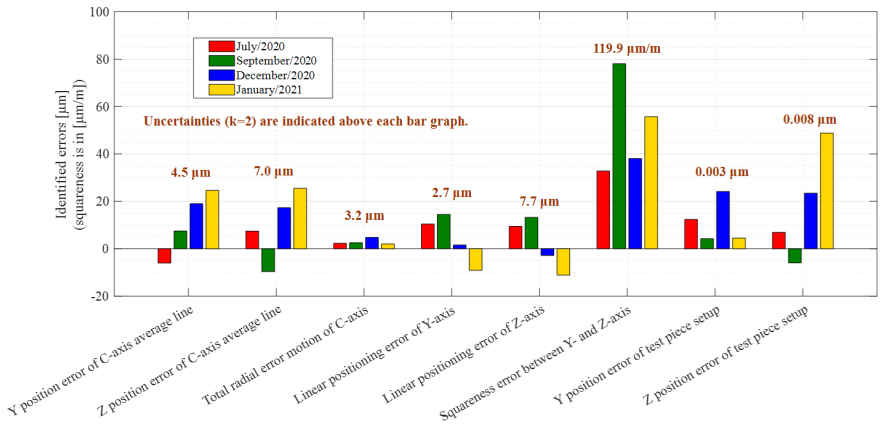

Figure 10: Geometric errors of rotary and linear axes and the test piece identified by Tests S at B = −90° (Red bar: Jul./2020, Green bar: Sep./2020, Blue bar: Dec./2020, Yellow bar: Jan./2021)

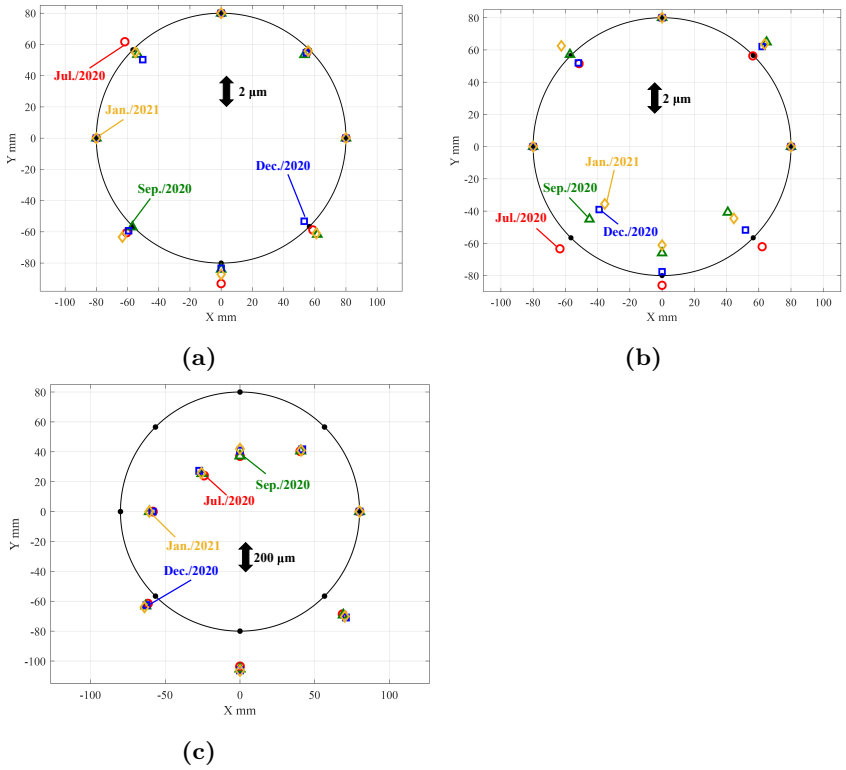

Figure 11: (a) The axial error motion of C-axis, $E_{ZC}(C_i, 0°)$. The black circle represents zero error. The error is magnified 10,000 times. (b) The positioning error of linear axes in the Z (axial) direction, $E_{ZC}(C_i, 0°)$. The black circle represents zero error. The error is magnified 10,000 times. (c) The shape deviation of the test piece in the Z direction, $W_{\text{axial}}(\theta_i)$. The black circle represents zero error. The error is magnified 100 times.

Fig. 8(c) shows the test piece geometric error, $W_{\text{radial}}(\theta_i)$. It is in the same polar plot format as in Fig. 8(b), with the error magnified 200 times. In the four tests, the same test piece was used. The change in Fig. 8(c) is mostly caused by the setup error of the test piece; the center of the best-fit circle to the trajectories in Fig. 8(c) represents the position error of the test piece's center to the machine tool's (X, Y) origin. Note that $W_{\text{radial}}(0°)$ is constrained to zero by Eq. (8)

(1-2) Error indices calculated from the identified errors

To numerically evaluate the change in rotary and linear axis error motions, error indices are calculated from the identified trajectories shown in Fig. 8. The definition of the error indices in Fig. 9 are in accordance with ISO 230-1 [26]. For example, they are calcurated as follows:

- The X and Y position errors of C-axis average line, represented by E_{X0C} and E_{Y0C} in ISO 230-1 [26]. are calculated as the center of the best-fit circle to the trajectory of $(E_{XC,\mathrm{total}}(C_i, 0°), E_{YC,\mathrm{total}}(C_i, 0°))$, shown in cross marks in Fig. 8(a). Their changes over half a year are shown in the first and second columns in Fig. 9.

- The total radial error motion of C-axis, defined in ISO 230-7 [8], is calculated as the difference in the maximum and minimum variation of $(E_{XC,\mathrm{total}}(C_i, 0°), E_{YC,\mathrm{total}}(C_i, 0°))$ from its best-fit circle. It is shown in the 3rd column in Fig. 9.

- Linear positioning errors of X- and Y-axes, represented by E_{XX} and E_{YY} in ISO 230-1 [26], are calculated from $E_{\mathrm{radial},XY}(\theta_i, 0°)$ at $\theta_i = 180°$ and $\theta_i = 270°$, respectively, in Fig. 8(b). They are shown in the 4th and 5th columns in Fig. 9.

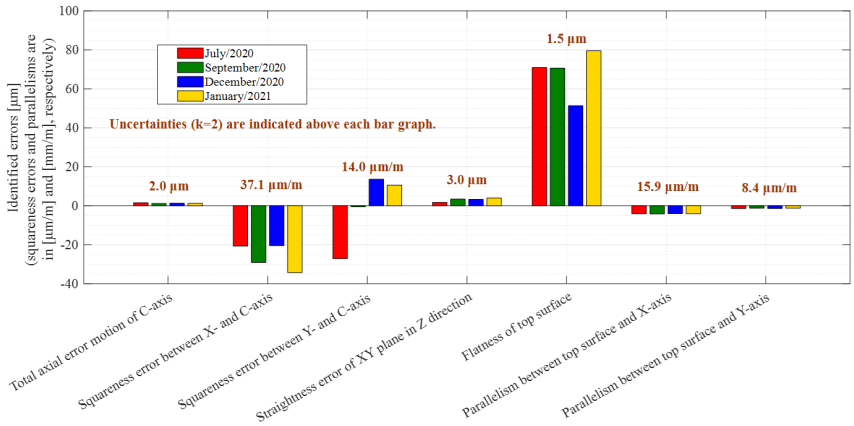

Figure 12: Geometric errors of rotary and linear axes and the test piece identified by Tests T at B = 0° (Red bar: Jul./2020, Green bar: Sep./2020, Blue bar: Dec./2020, Yellow bar: Jan./2021)

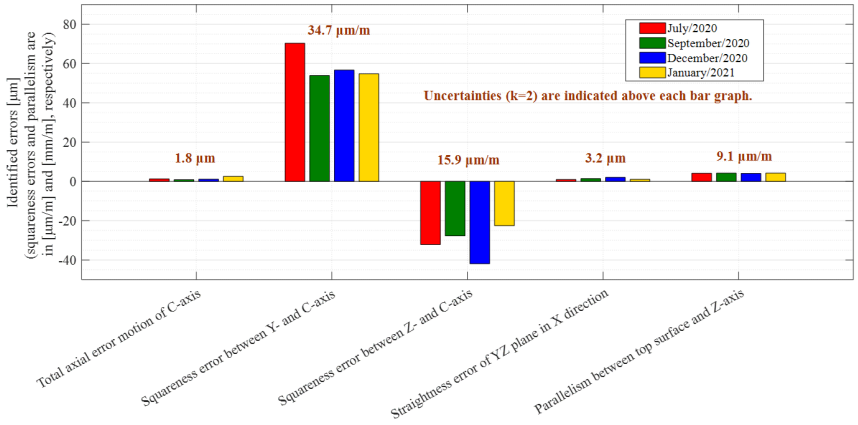

Figure 13: Geometric errors of rotary and linear axes and the test piece identified by Tests T at B = −90° (Red bar: Jul./2020, Green bar: Sep./2020, Blue bar: Dec./2020, Yellow bar: Jan./2021)

(2) Tests S at B = −90° (Probing tests for the side face with the table at vertical position)

Similarly at B = −90°, Tests 4-a-S to 6-S in Fig. 4 were performed (see Fig. 7(b)). By applying the algorithm presented in Section 4.1.2, Y-, Z- and C-axis and test piece geometric errors, defined in Table 3, were identified for B = −90°. Figure 10 summarizes the error incices calculated similarly as in (1). The followings can be observed:

- The position of the C-axis average line was changed at maximum by 30 μm and 30 μm in Y and Z direction, respectively.
- The squareness error of Z- to Y-axis was initially 33 μm/m in the first test (July 2020), and was changed by 45 μm/m at maximum during half a year, which is three times larger than the variation in the X-Y squareness error in Fig. 9.
- The linear positioning error of Y-axis was changed at maximum approximately by 20 μm, and the linear positioning error of Z-axis was smaller than that of Y-axis in each test.

(3) Tests T at B = 0° and B = −90° (Probing tests for the top face)

Tests 1-a-T to 3-T in Fig. 5 were performed at B = 0°. X-, Y- and C-axis and test piece geometric errors, defined in Table 4 were identified by applying the algorithm presented in Section 4.2.1. The black dots represent the nominal points, and the identified errors were shown in radial direction, magnified 10,000 times in Figs. 11(a) and 11(b), and 1,000 times in Fig. 11(c).

- In Fig. 11(a), the center offset of the identified $E_{ZC}(C_i, 0°)$ shows the squareness error of C- to X- or Y-axis. The C-axis axial error motion is the deviation from its best-fit circle. Both were sufficiently small in every test.

- In Fig. 11(b), the variation in the positioning error of linear axes in the Z-direction, $E_{ZZ}(C_i, 0°)$, was at maximum 4 μm within the four tests. Considering that the minimum positioning resolution of the machine tool is 1 μm, this variation is not significant.

- In Fig. 11(c), the shape deviation of the test piece in the Z direction, $W_{\text{axial}}(\theta_i)$, is mostly caused by the parallelism error of its top surface to the XY plane of the machine. The flatness of the top surface can be calculated as the deviation from the best-fit circle to the trajectory of $W_{\text{axial}}(\theta_i)$.

Figure 12 shows the error indices calculated from the identified errors in Fig. 11. Test T was performed also at B = ±90°. as presented in Sections 3.2.2 and 4.2.2. Figure 13 shows the error indices for Test T at B = −90°. The followings can be observed:

- The squareness errors of C- to X- and Y-axes at B = 0°, and to Y- and Z-axes at B = −90°, varied within the four tests, but their variation was not significant (for the test piece's nominal diameter 180 mm, its influence was up to about 5 μm).

6. Case Study #2: Performance check for thermal compensation

6.1. Test objective

The objective of Case study #2 is to demonstrate the application of the proposed scheme 1) to the observation of thermal influences on linear and rotary axis geometric errors, when a machine tool is in a temperature-controlled room and its room temperature is changed significantly, and 2) to the performance check of thermal compensation implemented in a commercial machine tool controller. The configuration of the machine tool is shown in Fig. 14.

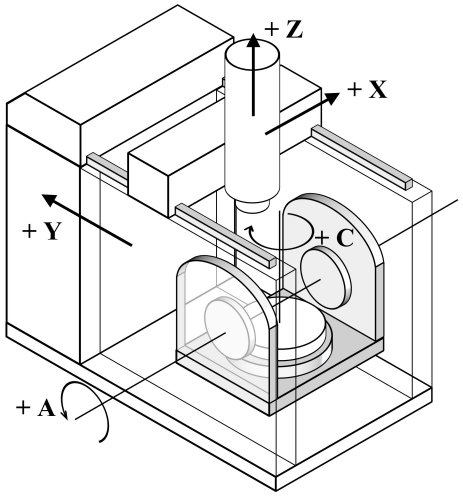

Figure 14: Configuration of the machine tool used in Case Study #2

6.2. Test setup and procedure

A cylindrical test piece (approximate size: diameter 500 mm, material: aluminum alloy, see Fig. 15) was measured on a vertical five-axis machining center. According to ISO 10791-2 [27], the kinematic chain of the machine tool is expressed as follows: V[w-C-A-b-Y-X-Z-(C)-t]. A touch-trigger probe, RMP400 by Renishaw, of the same measurement uncertainty as OMP400 (shown in Section 5.2), was used. The diameter of the stylus spheres was 6 mm.

The test procedure is as follows:

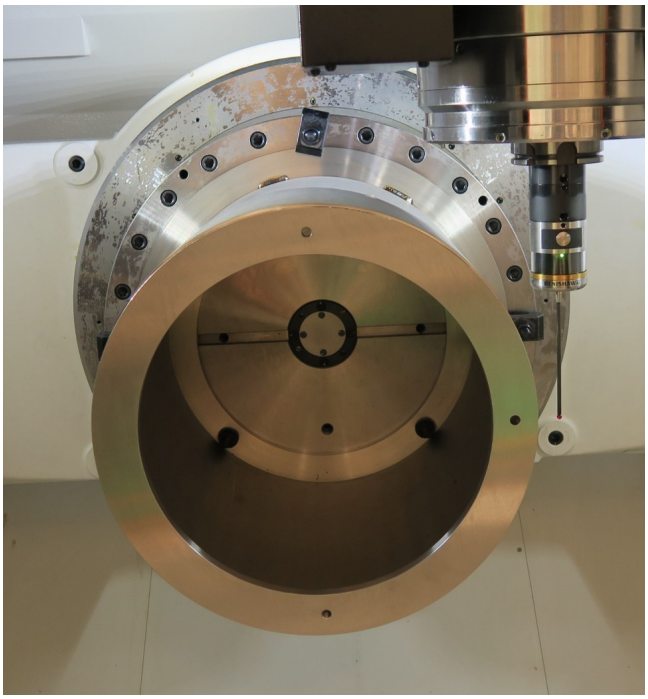

Figure 15: Test setup at A = −90°

1) The room temperature was regulated at 22 °C for a period sufficient to stabilize. Tests S, presented in Section 3.1, were conducted at A = 0° and A = −90° with the machine controller's thermal compensation turned off;

2) Room temperature was regulated at 30 °C for a period sufficient to stabilize, and then Tests S were conducted at A = 0° and A = −90° without thermal compensation; and

3) Under the same room temperature, the machine controller's thermal compensation was activated, and then Tests S were conducted at A = 0° and A = −90°. Before starting each step, the test piece was installed on machine table for a period sufficient to stabilize its temperature. The detailed functionalities of the thermal compensation in the machine controller are not disclosed. It is disclosed that multiple temperature sensors are installed at various locations in the machine structure. Numerical compensation based on some thermal error prediction model is implemented. The model, including its input/output dimen-

sions, e.g. the compensation for 3D position or Z error only, is not disclosed.

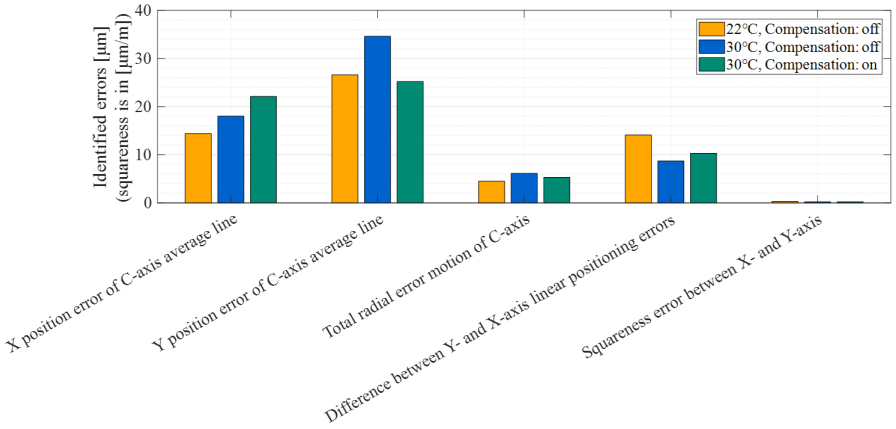

Figure 16: Geometric errors of rotary and linear axes and the test piece identified by Tests S at A = 0°

475

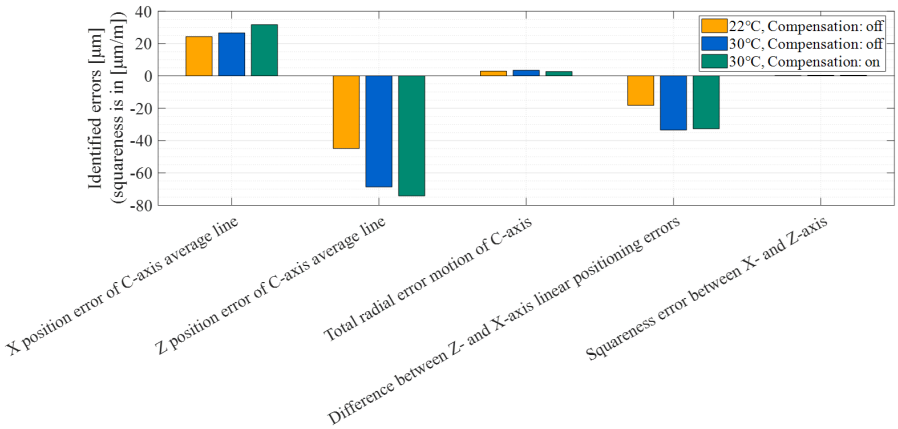

Figure 17: Geometric errors of rotary and linear axes and the test piece identified by Tests S at A = −90°

6.3. Test Results

(1) Observation of thermal influence

Figure 16 shows C-, X- and Y-axis geometric errors identified by Test S performed at A = 0°. The influence of the change in room temperature, from 22

°C to 30 °C, can be observed from orange ("22 °C, Compensation: off") and and blue ("30 °C, Compensation: off") bars. The followings can be observed:

- X and Y positions of C-axis average line moved to the positive direction by 4 μm and 8 μm, respectively.
- At 22 °C, the linear position error of Y-axis was larger than that of X-axis by 14 μm. When room temperature was changed to 30 °C, it was reduced to 9 μm.
- Squareness error between X- and Y-axis was sufficiently small both under 22 °C and 30 °C.

Similarly, Fig. 17 shows the errors identified by Test S performed at A = $-90°$. The followings can be observed:

- The Z-position of C-axis average line was displaced in the negative direction by 24 μm. This is likely attributable to the thermal displacement of the spindle to Z-direction. On the other hand, the displacement to the X-direction was only 2 μm, which is similar as the X-displacement observed at A = $0°$.
- At 22 °C, the linear position error of Z-axis was smaller than that of X-axis by 18 μm, and at 30 °C, this difference was increased to 33 μm. This is largely caused by thermal deformation of Z-axis.
- Squareness error between X- and Z-axis was sufficiently small both under 22 °C and 30 °C.

On this machine, the change in room temperature influenced the linear positioning error of all the linear axes. Since the position error of C-axis average line is defined with respect to the origin of linear axes, the C-axis position is thermally influenced in X- and Y-directions at A = $0°$, and in X and Z directions at A = $-90°$. The displacement was larger in the Z direction but existed both in X and Y directions.

(2) Performance check for thermal compensation

In Figs. 16 and 17, the performance of the thermal compensation, implemented in the machine controller, can be studied by comparing from blue ("30 °C, Compensation: off") and green ("30 °C, Compensation: on") bars. If thermal compensation works perfectly, the change in rotary or linear axis geometric errors caused by temperature change can be cancelled. In other words, in Figs. 16 and 17, green ("30 °C, Compensation: on") bars would be closer to orange ("22 °C, Compensation: off") bars, if thermal compensation works perfectly. The followings can be observed:

- Most typical thermal deformation would be in the Z-direction. Figure 17 shows that the Z position error of C-axis at $A = -90^\circ$ was not reduced by applying the thermal compensation.
- On the other hand, in Fig. 16, the Y position error of C-axis at $A = 0^\circ$ was reduced to the value at 22 °C by applying the thermal compensation. It shows the effectiveness of the compensation. The X-position error of C-axis was, however, not reduced.

The thermal compensation seemed effective only in the Y-direction. However, many geometric errors with respect to linear and rotary axes were not compensated.

7. Conclusion

The contributions of this paper can be summarized as follows:

- Many schemes in the literature, such as the R-test, the ball bar tests, and the probing-based tests, cannot separately identify rotary and linear axis geometric errors. Based on the self-calibration, this paper presented a novel on-machine measurement scheme to separately identify rotary and linear axis error motions by using a touch-trigger probe and an uncalibrated cylindrical artefact.

- Our preliminary work [23] proposed Test S (probing tests for the side face). This paper extended it to Test T, probing tests for the top face, to identify the axial error motion of C-axis and the Z-axis linear positioning error motion. It was furthermore extended to the tests with the machine table vertical, such that the C-axis error motions, as well as linear axis error motions, can be identified over the entire workspace.

- The proposed scheme is applicable to a periodic check of rotary and linear axis geometric errors, since it does not require a calibrated artifact. To demonstrate it, the case study was presented to observe long-term changes in rotary and linear axis error motions by periodically performing the proposed tests over six months.

- As the second experimental case study, the influence of room temperature change on linear and rotary axis error motions was observed. The performance of the thermal compensation implemented in a commercial machine tool controller was investigated by the proposed scheme.

The limitations of the present scheme include: 1) it cannot identify the angular positioning error of the C-axis. 2) the error motions of linear axes can be observed only in the radial direction of the test piece. Separate identification of straightness and angular error motions of linear axes is not possible. 3) The "absolute" linear positioning error of a linear axis cannot be identified by the self-calibration scheme, and thus its direct measurement is needed by probing a bar of the pre-calibrated length, 4) The machine's error motions are assumed unchanged during the proposed tests.

References

[1] K. Xing, S. Achiche, J.R.R. Mayer, Five-axis machine tools accuracy condition monitoring based on volumetric errors and vector similarity measures, Int. J. Mach. Tools Manuf. 138 (2019) 80-93.

[2] J. Mayr, J. Jedrzejewski, E. Uhlmann, M.A. Donmez, W. Knapp, F. Härtig, K. Wendt, T. Moriwaki, P. Shore, E. Schmitt, C. Brecher, T. Würz, K. Wegener, Thermal issues in machine tools, CIRP Ann. Manuf. Technol. 61(2) (2012) 771-791.

[3] M. Reuss, A. Dadalau, A. Verl, Friction Variances of Linear Machine Tool Axes, Procedia CIRP 4 (2012) 115-119.

[4] M. Hajdukiewicz, D. Byrne, M.M. Keane, J. Goggins, Real-time monitoring framework to investigate the environmental and structural performance of buildings, Build Environ. 86(Supplement C) (2015) 1-16.

[5] Y.Q. Wang, J.K. Wu, H.B. Liu, et al, Geometric accuracy long-term continuous monitoring using strain gauges for CNC machine tools, Int. J. Adv. Manuf. Technol. 98 (2018) 1145-1153.

[6] F. Aggogeri, A. Borboni, R. Faglia, A. Merlo, N. Pellegrini, A Kinematic Model to Compensate the Structural Deformations in Machine Tools Using Fiber Bragg Grating (FBG) Sensors, Appl. Sci. 7(2) (2017) 114.

[7] ISO 10360-2:2009: Geometrical product specifications (GPS) — Acceptance and reverification tests for coordinate measuring machines (CMM), Geneva.

[8] ISO 230-7: 2015. Test code for machine tools — Part 7: Geometric accuracy of axes of rotation.

[9] S. Ibaraki, W. Knapp, Indirect Measurement of Volumetric Accuracy for Three-Axis and Five-Axis Machine Tools : A Review, Int. J. Autom. Technol. 6(2) (2012)110-124.

[10] S. Weikert, W. Knapp, R-Test: a New Device for Accuracy Measurements on Five Axis Machine Tools, CIRP Ann. Manuf. Technol. 53(1) (2004) 429-432.

[11] S. Ibaraki, C. Oyama, H. Otsubo, Construction of an error map of rotary axes on a five-axis machining center by static R-test, Int. J. Mach. Tools Manuf. 51 (2011) 190-200.

[12] H. Cefu, S. Ibaraki, C. Oyama, Graphical presentation of error motions of rotary axes on a five-axis machine tool by static R-test with separating the influence of squareness errors of linear axes, Int. J. Mach. Tools Manuf. 59 (2012) 24-33.

[13] B. Bringmann, W. Knapp, Model-based 'Chase-the-Ball' Calibration of a 5-Axes Machining Center. CIRP Ann. Manuf. Technol. 55(1) (2006) 531-534.

[14] G.H.J. Florussen, H.A.M. Spaan, Static R-test: allocating the centerline of rotary axes of machine tools, In: Proceedings of the Eighth Lamdamap Conference. (2007) 196-202.

[15] M. Tsutsumi, A. Saito, Identification and compensation of systematic deviations particular to 5-axis machining centers, Int. J. Mach. Tools Manuf. 43(8) (2003) 771-780.

[16] J.R.R. Mayer, Five-axis machine tool calibration by probing a scale enriched reconfigurable uncalibrated master balls artefact, CIRP Ann. Manuf. Technol. 61(1) (2012) 515-518.

[17] S. Ibaraki, Y. Ota, Error Calibration for Five-Axis Machine Tools by On-the-Machine Measurement Using a Touch-Trigger Probe, Int. J. Autom. Technol. 8(1) (2014) 20-27.

[18] S. Ibaraki, T. Iritani, T. Matsushita, Error map construction for rotary axes on five-axis machine tools by on-the-machine measurement using a touch-trigger probe, Int. J. Mach. Tools Manuf. 68 (2013) 21-29.

[19] Y.T. Chen, P. More, C.S. Liu, Identification and verification of location errors of rotary axes on five-axis machine tools by using a touch-trigger probe and a sphere, Int. J. Adv. Manuf. Technol. 100 (2019) 2653-2667.

[20] B. Bringmann, W. Knapp, Machine tool calibration: Geometric test uncertainty depends on machine tool performance, Precis. Eng. 33(4) (2009) 524-529.

[21] ISO 230-2: 2014. Test code for machine tools — Part 2: Determination of accuracy and repeatability of positioning of numerically controlled axes.

[22] K.I. Lee, S.H. Yang, Measurement and verification of position-independent geometric errors of a five-axis machine tool using a double ball-bar, Int. J. Mach. Tools Manuf. 70 (2013) 45–52.

[23] N. Zimmermann, S. Ibaraki, Self-calibration of rotary axis and linear axes error motions by an automated on-machine probing test cycle, Int. J. Adv. Manuf. Technol. 107(5-6) (2020) 2107-2120.

[24] C.J. Evans, R.J. Hocken, W.T. Estler, Self-Calibration: Reversal, Redundancy, Error Separation, and 'Absolute Testing', CIRP Ann. Manuf. Technol. 45(2) (1996) 617-634.

[25] E.R. Marsh, D.A. Arneson, D.L. Martin, A comparison of reversal and multiprobe error separation, Precis. Eng. 34(1) (2010) 85-91.

[26] ISO 230-1: 2012. Test code for machine tools — Part 1: Geometric accuracy of machines operating under no-load or quasi-static conditions.

[27] ISO 10791-2: 2001. Test conditions for machining centres Part 2: Geometric tests for machines with vertical spindle or universal heads with vertical primary rotary axis, International Organization for Standardization ISO, Geneva, Switzerland.

[28] ISO 230-4:2005. Test code for machine tools — Part 4: Circular tests for numerically controlled machine tools.